IEEE Access
Multidisciplinary : Rapid Review : Open Access Journal

Date of publication xxxx 00, 0000, date of current version xxxx 00, 0000.

Digital Object Identifier 10.1109/ACCESS.2024.Doi Number

Improved Analytical Model for Axial Flux Permanent-Magnet Machine by Current Sheet Method

Qilong Xue [1], Pengpeng Huang [2], Frédéric Dubas[3] and Baocheng Guo [2]
[1] China University of Geosciences Beijing, Beijing, China
[2] School of School of Electrical and Automation Engineering, Nanjing Normal University, Nanjing, China
[3] Université Marie et Louis Pasteur, UTBM, CNRS, Institut FEMTO-ST, F-90010 Belfort, France

Corresponding author: Pengpeng Huang (e-mail: 545622078@qq.com).

ABSTRACT This paper presents a novel sub-domain (SD) model is presented, based on current sheet method, to reduce the order of solving matrix and computational time significantly. The permanent magnets (PMs) of axial flux permanent magnet (AFPM) machines are modeled by pairs of coils on each side of PMs in Cartesian coordinates. With the proposed method, PMs and the air-gap in the subdomain model are combined into a single region, resulting in a reduced-order solving matrix. The proposed analytical model is thoroughly described, presenting its theoretical derivation. To validate the efficacy of the model, an AFPM machine is employed and comparison is made for magnetic flux densities and the magnetic performance. Remarkably, the FEM findings align closely with the outcomes derived from the proposed method. By leveraging this theory, engineers can accurately model a diverse range of PM shapes using a low-order matrix, ensuring high accuracy.

INDEX TERMS Axial Flux Permanent Magnet Machine (AFPM), Subdomain Modeling, Current Sheet Method, Reduced-Order Matrix, Analytical Electromagnetic Modeling.

NOMENCLATURE

J_s	equivalent current density;
M	magnetization vector;
J_1	equivalent surface current density;
H_{cj}	coercitive magnetic field;
A	magnetic vector potential;
R_m	equivalent radius;
i_c	the current in the equivalent of coil;
$A_{m1} \sim D_{m1}$	the unknown coefficients;
ρ	the length between ρ_α and ρ_β;
a	the height of discrete coil;
ζ	the span angle of the coil;
m, n	the harmonic order;
Δl	the length in the out sides of PM;
J_x	the current density on the sides x;
n_{sl}	the number of the slices;
t_{cp}	the slice width;
b_{so}	the slot-opening;
$\mathbf{n}$	the unit normal vector of the PM surface;

I. INTRODUCTION

PM electrical machines, which have compact structure, higher power/torque density and efficiency, are widely used in many industrial and military products, such as electric vehicles, hybrid electric vehicles and servo systems[1]. Different types of PM machines – like radial-flux PM (RFPM) [2], AFPM [3], and linear PM (LPM) machines [4] – are selected, designed and optimized according to the working space and requirement. For instance, in servo motors [4]-[6], a lower torque ripple is always required to improve the operation precision and dynamic response.

Significant work on the prediction of magnetic performance in PM electrical machines has been done in scientific literature. Numerical methods such as the finite element model (FEM) are widely adopted due to their ability to account for the complex structure and provide accurate results. However, FEM always consumes a long computational time and requires high CPU resources, hence, it is a good tool for design validation, but not a good approach for the initial design and optimization [7].

The alternative approach is the (semi-) analytical method, which is a good realistic model that can provide insights into geometric parameters and output performance characteristics. Furthermore, the efficient performance evaluation makes it suitable for optimization procedures. Recently, several studies have been conducted, focusing on the development and implementation of the two-dimensional (2-D) SD approach [9], [10], [11]. These authors have developed exact analytical solutions for PM electrical machines with conventional PM shape by using the Dubas' principle [8], [9]. For instance, Farrokh combined the simple equivalent magnetic circuit and analytical model to evaluated the magnetic performance of AFPM machine[10], [11]. In [12]-[13], the PM rotor with Halbach arrays is modeled for RFPM and AFPM machines, respectively. As for the shapes of PMs, the PMs are regarded as multi-small slices in [14], and the final magnetic flux densities excited by rectangle or bread loaf types of PMs are obtained by the principle of superposition. It is important to note that the accuracy of the results is highly dependent on the number of slices used, and finding the right balance between accuracy and CPU time is crucial. Alterative works on modeling the shape of PMs appeared in [15], the eccentric PM is modeled by two pairs of coils on the surface of the PM. Therefore, the PM can be expressed in a simple way in the SD model. Further work is presented in [16], where the local demagnetization is considered. Moreover, this method can combine the air-gap and PM regions together, which means that the unknown coefficients in the solving matrix are reduced, resulting in a lower computational time [15]-[16]. This SD model is a powerful approach to predict the mapping of the magnetic flux density in the PM electrical machine with different shapes of PMs. However, this model is only developed in polar coordinates for RFPM machines.

From the literature survey, the mathematic derivations of PMs with pairs of coils in Cartesian coordinates are not presented until now since the different Maxwell equations. In this paper, the first exact analytical solution for rectangle types of PMs is developed in Cartesian coordinates. The proposed model is a development based on the current sheet. Afterwards, a SD model for AFPM machines is modeled. PMs and the air-gap in the SD model are combined into a single region, resulting in a reduced-order solving matrix. The magnetic flux density in the air-gap and magnetic performance are validated by FEM results.

The structure of this paper is outlined as follows. Section II explores the general model for permanent magnets (PMs). Also, the current sheet on each side of PMs in Cartesian coordinates is given. Based on the theory, the analytical models of AFPM machine in Cartesian coordinates are developed in Section III. PMs and the airgap are combined as one in the SD model. Moreover, the geometrical parameters of the AFPM machine are given in Section IV. The results obtained by the FEM have verified the theory further in Section V. Finally, conclusive remarks are provided at the conclusion of this paper.

II. PERMANENT-MAGNET MODELING

This paper employs the analytical method to model the permanent magnets PMs utilized in the study. Typically, PMs are assumed to possess linear properties and exhibit uniform magnetization. In this case, the relative recoil permeability (μ_r) is assigned a value of 1.

Regarding the PMs, their magnetic field can be represented by two equivalent surface currents. In the two-dimensional (2-D) model adopted in this study, these two equivalent current densities can be mathematically expressed as [21].

$$J_S = \mathbf{M} \times \mathbf{n} \tag{1}$$

where **n** is the unit normal vector of the PM surface, and **M** is the magnetization vector of the PMs.

The equivalent surface current can be calculated by the circumferential component of coercivity ***Js*** according to the magnetization theory of the magnetic medium. Substituting the current density distributions with the discrete equivalent line currents, as shown in Fig. 1, an equivalent coil is introduced, and the current in the coil is called magnetizing current.

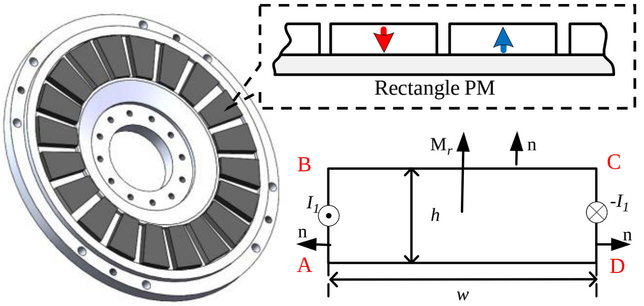

FIGURE 1. AFPM machine with PMs and pair of coils in rectangle PMs.

In the case of the rectangular PM, as illustrated in Figure 1, the vector **M** aligns parallel to the vector **n** on the top and bottom surfaces, resulting in **M**×**n** = 0. Consequently, there are no equivalent surface currents present on the BC and CD sides. Additionally, since **M** is orthogonal to the lateral sides, the equivalent surface current density J_1 is equal to ±|**M**|. Therefore, the surface current density on sides AB and CD can be expressed as follows:

$$J_1 = H_{cj} \tag{2}$$

where H_{cj} is the coercitive magnetic field of the PM.

It can be seen from the current equation in this section, revealing that various shapes of permanent magnets (PMs) can be effectively substituted with pairs of coils. The PM does not need to segment into pieces, hence, simplifying the calculation.

This article has been accepted for publication in IEEE Access. This is the author's version which has not been fully edited and
content may change prior to final publication. Citation information: DOI 10.1109/ACCESS.2025.3618398

III. ANALYTICAL CALCULATION

In this section, the analytical model with the equivalent PMs is applied to the original AFPM machine. The basic assumptions are:

1) Ignoring the saturation effect, it is assumed that the iron material has infinite permeability.
2) Losses stemming from the conversion process are disregarded in the analysis.
3) Ignoring eddy current loss and end effect.
4) The permanent magnet (PM) material is assumed to possess uniform magnetization, and its relative recoil permeability (μ_r) is taken as 1.

To simplify the calculations, the original AFPM machine considers the slots to be open slots without tooth-tips, as depicted in Fig.2. In the figure, the variables z and θ represent the height and angle, respectively. This simplification allows for easier analysis and modeling of the machine's characteristics. PMs and the airgap are combined as Region I. The theoretical derivation will be explained in detail further.

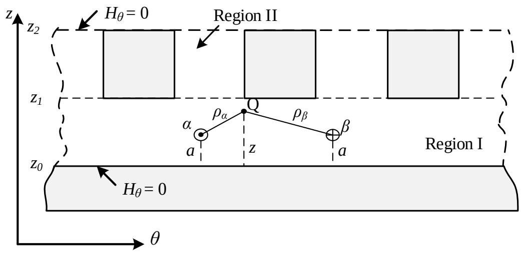

FIGURE 2. **Illustration of simple SD model.**

A. Model in Region I

In calculation Region I (viz., PMs and the air-gap), the 2-D magnetic vector potential $\boldsymbol{A}$ in Cartesian coordinates is governed by

$$\frac{\partial^2 A}{\partial z^2} + \frac{1}{R_m^2}\frac{\partial^2 A}{\partial \theta^2} = 0 \tag{3}$$

By employing the separation of variables method, the general solution for equation (5) is derived. Incorporating the coils into the analysis, the magnetic vector potential (A_{z1}) at point Q (as shown in Figure 2) is expressed as follows:

$$A_{z1} = -\frac{\mu_0 i_c}{2\pi}\rho + \sum_m \left[\left(A_{m1} e^{\frac{m}{R_m}z} + B_{m1} e^{-\frac{m}{R_m}z} \right)\cos(m\theta) \right] + \sum_m \left[\left(C_{m1} e^{\frac{m}{R_m}z} + D_{m1} e^{-\frac{m}{R_m}z} \right)\sin(m\theta) \right] \tag{4}$$

where i_c is the current in the equivalent of coil, m is the harmonic order in calculation Region I and R_m is the equivalent radius, A_{m1} to D_{m1} are the unknown coefficients need to be determined, and ρ is the length which is calculated by

$$\rho = \rho_\alpha - \rho_\beta \tag{5}$$

where ρ_α and ρ_β are the coordinates of point Q when the origin points are α and β, respectively. Further, ρ can be expanded into infinite series about z and θ

$$\rho = \begin{cases} -2\sum_m \frac{1}{m} e^{\frac{m}{R_m}(z-a)} \sin(m\zeta)\sin(m\theta), & z < a \\ -2\sum_m \frac{1}{m} \sin(m\zeta)\sin(m\theta), & z = a \\ -2\sum_m \frac{1}{m} e^{\frac{m}{R_m}(a-z)} \sin(m\zeta)\sin(m\theta), & z > a \end{cases} \tag{6}$$

where a is the height of discrete coil, and ζ is the span angle of the coil, which can be expressed by the pole-arc ratio.

The tangential and normal tangential components of $\boldsymbol{B}$ can be defined by

$$B_n = \frac{1}{R_m}\frac{\partial A}{\partial \theta}, \quad B_t = -\frac{\partial A}{\partial z} \tag{7}$$

For $z < a$, the tangential component of $\boldsymbol{H}$ is given by

$$H_{\theta,z1} = -\frac{\mu_0 i_c}{2\pi}\rho + \sum_m \left[\frac{m}{R_m}\left(A_{m1} e^{\frac{m}{R_m}z} - B_{m1} e^{-\frac{m}{R_m}z} \right)\cos(m\theta) \right] + \sum_m \left[\frac{m}{R_m}\left(C_{m1} e^{\frac{m}{R_m}z} - D_{m1} e^{-\frac{m}{R_m}z} \right)\sin(m\theta) \right] \tag{8}$$

Considering the tangential component in the outer rotor surface (i.e., $z = z_0$) is 0, the B_{m1} and D_{m1} can be expressed by

$$B_{m1} = A_{m1} e^{\frac{m}{R_m}2z_0} \tag{9}$$

$$D_{m1} = C_{m1} e^{\frac{m}{R_m}2z_0} + \frac{R_m}{m}\frac{\mu_0 i_c}{\pi}\frac{e^{\frac{m}{R_m}2z_0}}{e^{\frac{m}{R_m}a}}\sin(m\zeta) \tag{10}$$

For $z > a$, substituting (11) and (12) into (6), the general solution in Region I can be deduced as

$$A_{z1} = \sum_m \left[(A_{m1}G_{1m})\cos(m\theta) \right] + \sum_m \left[\left(C_{m1}G_{1m} + G_{0m} e^{-\frac{m}{R_m}z} \right)\sin(m\theta) \right] \tag{11}$$

where

$$G_{1m} = e^{\frac{m}{R_m}z} + e^{\frac{m}{R_m}2z_0} e^{-\frac{m}{R_m}z} \tag{12}$$

$$G_{0m} = \frac{\mu_0 i_c}{m\pi}\frac{e^{\frac{m}{R_m}2z_0} + e^{\frac{m}{R_m}2a}}{e^{\frac{m}{R_m}a}}\sin(m\zeta) \tag{13}$$

The magnetic vector potential produced by the equivalent coil of j-th PM, (13) is given by

$$A_{z1} = \sum_m \left[(A_{m1}G_{1m})\cos\{m[\theta + (j-1)\pi/P]\} \right] + \sum_m \left[\left(C_{m1}G_{1m} + G_{0mj} e^{-\frac{m}{R_m}z} \right)\sin\{m[\theta + (j-1)\pi/P]\} \right] \tag{14}$$

This article has been accepted for publication in IEEE Access. This is the author's version which has not been fully edited and content may change prior to final publication. Citation information: DOI 10.1109/ACCESS.2025.3618398

where

$$G_{0mj}=(-1)^{j-1}\frac{\mu_0 i_c}{m\pi}\frac{e^{\frac{m}{R_m}2z_0}+e^{\frac{m}{R_m}2a}}{e^{\frac{m}{R_m}a}}\sin(m\zeta) \quad (15)$$

B. Model in Region II

In Region II (viz., the slots), ***A*** in Cartesian coordinates is governed by

$$\frac{\partial^2 A}{\partial z^2}+\frac{1}{R_m^2}\frac{\partial^2 A}{\partial \theta^2}=-\mu_0 J_i \quad (16)$$

As it is well known, the magnetic field in Region II is symmetrical about the symmetrical line in the slot, the general solution in Region II is

$$A_{2i}=A_{\theta p}(z,\theta)+\sum_n(A_n e^{\frac{E_n}{R_m}z}+B_n e^{-\frac{E_n}{R_m}z})\cos\left[\frac{E_n}{R_m}\left(\theta+\frac{b_{so}}{2}\right)\right] \quad (17)$$

where E_n equals to $n\pi/b_{so}$ with n is the harmonic order in Region II and b_{so} is the slot-opening.

The tangential component of ***H*** is given by

$$H_{\theta 2i}=\sum_n\frac{E_n}{R_m}(A_n e^{\frac{E_n}{R_m}z}-B_n e^{-\frac{E_n}{R_m}z})\cos\left[\frac{E_n}{R_m}\left(\theta+\frac{b_{so}}{2}\right)\right] \quad (18)$$

Considering the tangential component in line z_2 is zero, the normal component of ***B*** can be expressed by

$$B_n=A_n e^{\frac{E_n}{R_m}2z_3} \quad (19)$$

Substituting (21) into (19), the general solution in Region II can be deduced as

$$A_{2i}=\frac{1}{2}\mu_0 J_i\left[(z_1^2-z^2)+2z_2^2\ln\left(\frac{z}{z_1}\right)\right]$$
$$D_{n2i}\left(G_{4n}e^{\frac{E_n}{R_m}(z-z_2)}+e^{\frac{E_n}{R_m}(z_1-z)}\right)\cos\left[\frac{E_n}{R_m}\left(\theta+\frac{b_{so}}{2}\right)\right] \quad (20)$$

where D_{n2i} is the new unknown coefficient obtained by scalar approach, and

$$G_{4n}=e^{\frac{E_n}{R_m}(z_1-z_2)} \quad (21)$$

C. Connection between Two Regions

According to the distribution of ***A*** in calculation Region I, the tangential component of ***B*** in the line z_2 can be calculated as

$$\left.\frac{\partial A_I}{\partial z}\right|_{z=z_2}=\begin{cases}\left.\frac{\partial A_i}{\partial z}\right|_{z=z_2} & \forall\theta\in[\theta_i,\theta_i+\beta]\\ 0 & elsewhere\end{cases} \quad (22)$$

which leads to

$$\frac{m}{R_m}[A_{m1}G_{2m}]=\frac{2}{2\pi}\sum_{i=1}^{Q}\int_{\theta_i}^{\theta_i+\beta}\left.\frac{\partial A_i}{\partial z}\right|_{z_2}\cos(m\theta)d\theta \quad (23)$$

$$\frac{m}{R_m}[C_{m1}G_{2m}]-\frac{m}{R_m}\left(G_{0m}e^{-\frac{m}{R_m}z1}\right)=\frac{2}{2\pi}\sum_{i=1}^{Q}\int_{\theta_i}^{\theta_i+\beta}\left.\frac{\partial A_i}{\partial z}\right|_{z_2}\sin(m\theta)d\theta \quad (24)$$

According to the magnetic flux continuity condition, the distribution of ***A*** in the side of $_{z2}$ can be given as

$$A_i|_{z=z_2}=A_I|_{z=z_2} \quad (25)$$

which leads to

$$D_{n2i}\left(G_{4n}e^{\frac{E_n}{R_m}(z-z_3)}+e^{\frac{E_n}{R_m}(z_2-z)}\right)=\frac{2}{b}\int_{\theta_i}^{\theta_i+\beta}A_I\cos\left[\frac{E_n}{R_m}(\theta+b_n/2)\right]d\theta \quad (26)$$

According to (26) to (28), there are 3 equations and 3 unknown coefficients, the solving matrix format can be given as

$$\begin{bmatrix}K_{11}&0&K_{13}\\0&K_{22}&K_{23}\\K_{31}&K_{32}&K_{33}\end{bmatrix}\begin{bmatrix}A_{m1}\\C_{m1}\\D_{n2i}\end{bmatrix}=\begin{bmatrix}J_1\\Y_2+J_2\\Y_3\end{bmatrix} \quad (27)$$

where K_{11} to K_{13} are the coefficients, and Y_2 & Y_3 are sources.

D. Superposition of Magnetic Vector Potential

The current in the coil (i_c), can be equivalent to the sum of the current in each line, and can be calculated.

$$i_c=J_x\Delta l \quad (28)$$

where Δl is the length in the out sides of PM, and J_x is the current density on the sides x.

The magnetic vector potential (***A***) generated by the current flowing through sides AB and CD can be determined through appropriate mathematical calculations.

$$A_{z11}=\sum_k A_{z1}|_{\substack{z=z_0+k_1\triangle h\\ i_c=J_1\triangle h}} \quad (29)$$

Further, the coil current in Fig. 3(a) can be given by

$$i_1=J_{s1}\Delta z=\int_{z_0}^{z_1}J_{s1}da \quad (30)$$

As for the trapezoidal PM, *A* produced by the equivalent surface current of side BE and CF is defined by

$$A_{z11}=\sum_k A_{z1}|_{\substack{z=z_1+\triangle h\\ i_c=J_2\triangle h\sin\alpha}} \quad (31)$$

The winding current i_2 in Fig. 3(b) is

$$i_2 = J_2 \frac{dh}{\sin\alpha} = \int_{z_0}^{z_1} J_{s2} da \tag{32}$$

Finally, the calculation of $\boldsymbol{A}$ for each side can be performed independently. By employing the principle of superposition, both the normal and tangential components of $\boldsymbol{B}$ can be determined separately.

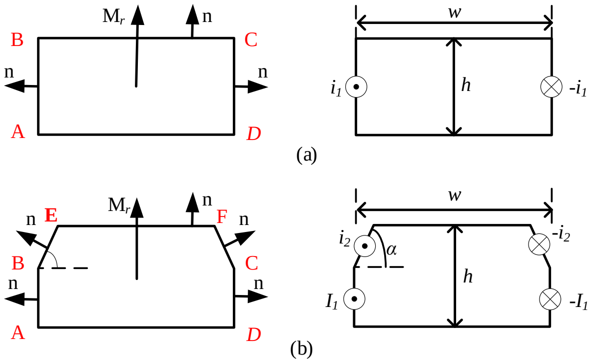

FIGURE 3. PM model. (a) rectangle. (b) trapezoidal chamfer.

IV. MODEL DESCRIPTION

The chosen configuration for demonstrating the proposed coordinate transformation process is an AFPM machine with a yokeless and segmented armature (YASA) topology. This machine consists of two rotors and one stator, as depicted in the three-dimensional (3-D) AFPM model shown in Fig. 4(a). Detailed dimensions and parameters of this machine can be found in Table I.

TABLE I
MAIN DIMENSIONS AND PARAMETERS OF THE AFPM MACHINE.

Parameters	Value	Parameters	Value
Inner diameter D_i	67.8mm	Pole pairs p	5
Outer diameter D_o	105mm	Remanence of PM B_r	1.07 T
Air-gap length g	2.2 mm	PM thickness h	1.7 mm
Slots	12	Width of slot t_{s2}	12.6mm
Height of slot h_{s1}	2.8mm	Height of rotor iron h_{rb}	6mm
Height of stator h_{s2}	11.5mm	Slot-opening width	2.5mm

Typically, the quasi-3D method is commonly utilized to convert a 3-D model into a 2-D model, aiming to reduce computational time. In the case of the AFPM machine, it is divided into multiple layers, each having a cylindrical cross-section. By employing this approach, the machine can be represented by several 2-D calculation planes, as illustrated in Fig. 4(b). The adoption of such decomposition allows for simulating partial demagnetization of the permanent magnets at different locations, thereby achieving more accurate results. For a specific layer, the average radius Rave can be determined using the following expression:

$$R_{ave}^k = R_i^a + \frac{R_o^a - R_i^a}{2n_{sl}}(2k-1),\ k = 1, 2, ..., n$$
$$t_{cp} = \frac{R_o^a - R_i^a}{n_{sl}} \tag{33}$$

where n_{sl} is the number of the slices, and t_{cp} is the slice width.

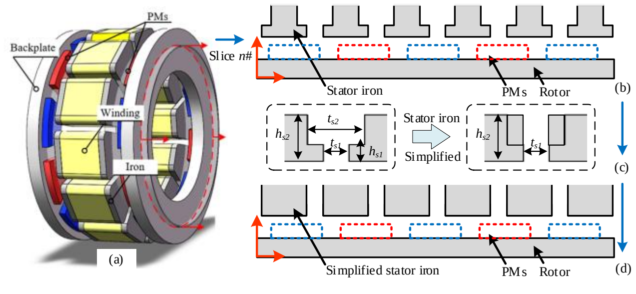

FIGURE 4. The AFPM machine with 12-lots/10-poles.

In this paper, to simplify the analysis, the slot geometry is simplified. The original structure of 2-D model is shown in Fig. 4(c), the slot width is simplified as the same as the slot-opening width, it can reduce the complexity of the analytical model while maintaining high accuracy. The final 2-D model is illustrated in Fig. 4(d).

To validate the proposed analytical solution, the AFPM machine with three types of PM are modeled. The PM in machine has a rectangle shape as shown in Table II.

TABLE II
GEOMETRICAL PARAMETERS OF PM

Parameters	Machine I	Machine II
Air-gap length g	2.2 mm	2.2 mm
PM thickness (min) h	1.7 mm	1.7 mm
PM thickness (max) h	1.7 mm	2.5 mm
Angle α	0	15 degree

V. FINITE-ELEMENT VALIDATIONS

Building upon previous research, a FEM model with non-linear magnetic iron is developed in this study. This model enables the calculation of air-gap magnetic flux densities, back electromotive force (EMF), and torque. In this section, we will compare the normal and tangential components of the magnetic field vector $\boldsymbol{B}$ in the air-gap, as well as analyze the overall magnetic performance of the proposed analytical model. To simplify the calculation, a 1/4 model is established. Fig. 5 shows the no-load magnetic field distribution of the 2-D model.

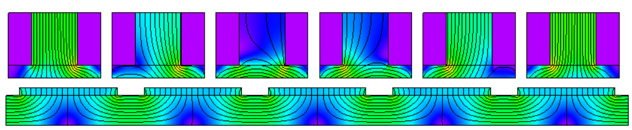

FIGURE 5. The flux density distribution of AFPM with rectangle PM shape.

From the simulation results, the maximum of flux density is 1.4T, which is working under un-saturation condition. Normally, the rated working point of iron is designed under knee point, which has little influence on the results of AM. However, the flux densities will change significantly when the machine works under extreme operating conditions. The permeability of iron, especially the shoe region, would very small and result in inhibiting growth of air gap flux densities, but the AM assume that the permeability is infinite, which may lead to higher flux density and torque. This can be solved by combining the simple magnetic circuit to consider the nonlinear properties of iron [19].

A. Magnetic Flux Density: Rectangle Shape

The normal and tangential components of B for machine with a rectangle shape of PMs under the open circuit are shown in Fig. 6(a) and Fig. 6(b). The equivalent models are matched with FEM. The harmonic spectrum of the normal component is shown in Fig. 6(c). The basic harmonic of analytical model is a little lower than that of FEM, this is mainly caused by the saturation effect and simplification. The agreement results validate the correctness of the model, also the current for the sides AB and CD. The THD is around 24% for the rectangle shape of PMs.

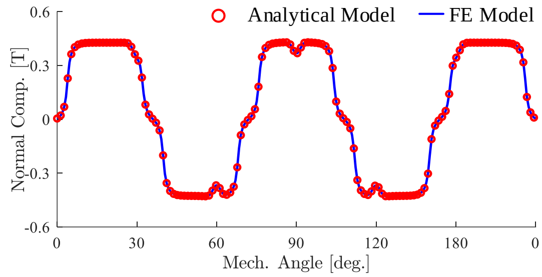

(a)

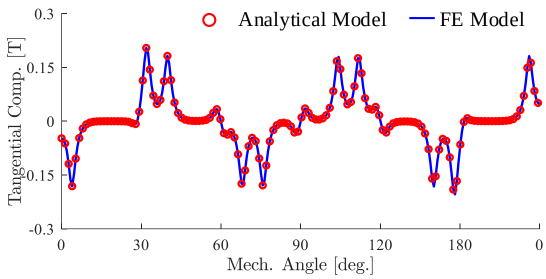

(b)

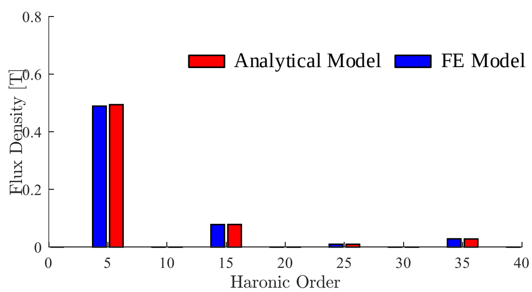

(c)

FIGURE 6. The normal and tangential component of the open-circuit magnetic flux density in the air-gap (rectangle shape of PMs). (a) Normal Waveform. (b) tangential waveform. (c) Harmonic spectrum.

B. Magnetic Flux Density: Trapezoidal Chamfer Shape

The various components of B for Machine II with trapezoidal chamfer shape of PMs, is shown in Fig. 7(a) and Fig. 7(b). The agreement is also obtained by comparing it with FEM. It should be noted that the PM height is higher than the rectangle PM, hence, the amplitude of flux densities is higher. It can be deduced that the current of the PM sides is correct. The harmonic spectrum of the normal component for Machine II is shown in Fig. 7(c), respectively. The harmonics of analytical model are also matched. The THD is around 19.1% for rectangle shape and 13.9% for the trapezoidal chamfer shape of PMs.

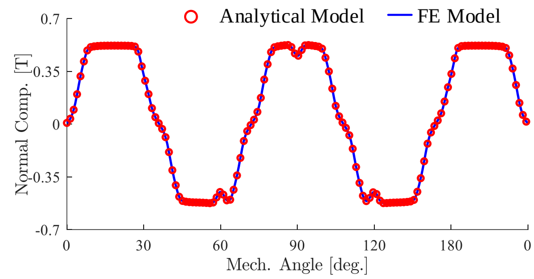

(a)

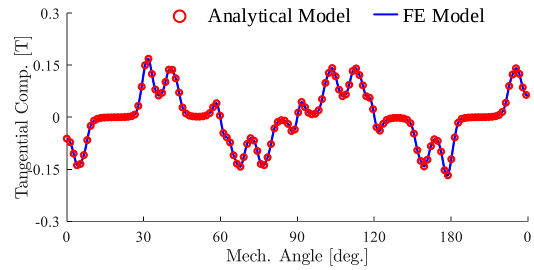

(b)

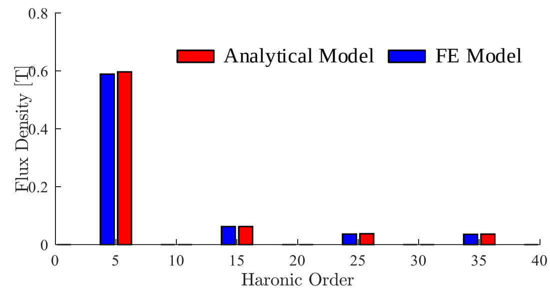

(c)

FIGURE 7. The normal and tangential component of the open-circuit magnetic flux density in the air-gap for Machine II (viz. trapezoidal chamfer shape of PMs). (a) Normal Waveform. (b) tangential waveform. (c) Harmonic spectrum.

C. Magnetic Performances Comparison

According to the Maxwell's stress tensor method, the torque T_{torq} can be computed by

$$T_{torq} = \frac{L_{stk} R^2{}_{calc}}{\mu_0} \int_0^{2\pi} B_n B_t d\theta \tag{34}$$

The cogging force is shown in Fig. 8 for different shapes of PMs and a good agreement with the FEM result is achieved.

Calculating the back EMF involves determining the total magnetic flux linkage of a single phase. This can be achieved by summing the fluxes of all coils within that phase. To evaluate the back EMF for a given electric angular speed (n_{sp}), Stoke's theorem is employed, which enables the calculation of the back EMF using the following methodology:

$$E_{phase,i} = n_{sp} \frac{d\varphi_{phase,i}}{dt} \tag{35}$$

where $E_{phase,i}$ is the back EMFs of phase i, $\varphi_{aphase,i}$ is the magnetic flux linkage of phase.

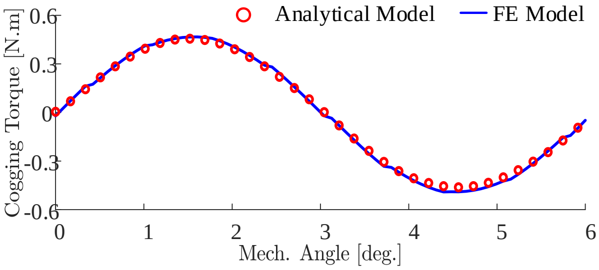

FIGURE 8. Cogging Torques.

The flux linkages are shown in Fig.9 (a). It can be observed that these results match well. Fig.9 (b) showcase the EMF results obtained from both the FE model and the proposed method. It is evident that the overall conversion theory demonstrates considerable accuracy in predicting the back EMF. However, slight discrepancies are observed between the results, which can be attributed to the minimal saturation effects under open conditions.

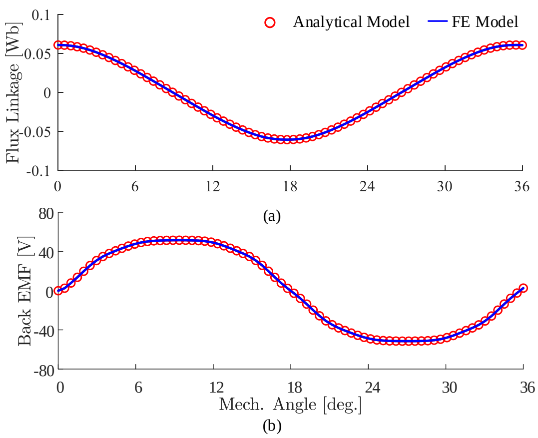

FIGURE 9. Comparison of magnetic flux linkage (a) and back EMF of phase *i* (b).

D. Computation Time Comparison

As for the computation time, it should be noted that the solution time is determined by the size of the solution matrix, which means that the harmonic order set in the model is very important. To compare the time, we set the spatial harmonic order in the air gap is M = 200, and N = 50 in the slot region.

To show the advantages of proposed model, the traditional SD model shown in [20] is adopted to compare with proposed method, as shown in Tab. III. Traditional SD model has 2 unknown coefficients in the PM region, 4 unknow coefficient in the airgap region and 1 unknown coefficient in the slot region. Hence, the total unknown coefficient is 6*M+12*N =1800, and the size of solving matrix is 1800 ×1800. Nevertheless, it only has 2 unknown coefficients in airgap and 1 unknown coefficient in slot region. Therefore, the total unknown coefficient is 2*M+12*N =1000, and the size of solving matrix is 1000 ×1000. The solving matrix is reduced almost half and the computation time is reduced from 0.32 to 0.22 seconds. It is important to recognize the significant engineering application value of the proposed model, particularly in optimization scenarios. By incorporating the proposed model with advanced algorithms such as the Non-dominated Sorting Genetic Algorithm II (NSGA-II), it becomes possible to achieve substantial reductions in overall calculation time.

TABLE III
COMPARISON WITH TRADITIONAL SD MODEL.

	Matrix Size	CPU Time	Accuracy
Proposed Model	1000×1000	0.22 s	Same
Traditional Model	1800 ×1800	0.32 s	Same

VI. EXPERIMENT

In order to further validate the conversion theory, the prototype machine is developed as shown in Fig. 10. The stator iron is fixed by electrical potting compound, and the PMs are fixed by glue. As for the test platform, to test the line/phase back electromotive force (EMF) with accuracy speed, the servo motor driving the AFPM prototype, this ia also shown in Fig. 10.

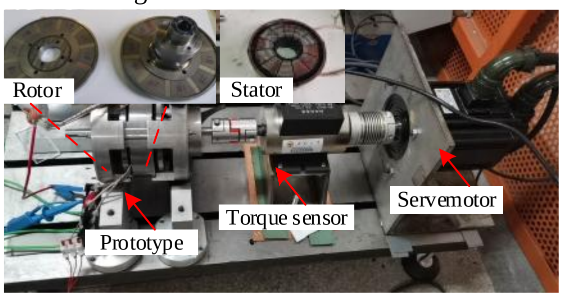

FIGURE 10. Experimental test platform.

The line back electromotive force (EMF) for each phase at a rotational speed of 1,000 rpm was conducted, and an oscilloscope was employed to measure and record the waveforms, shown in Figure 11(a). A comparison between the measured line back EMF and the results of the proposed method is shown in Figure 11(b). The Root Mean Square (RMS) value of the test is 40 V, compared with the 40.7 V obtained by proposed model.

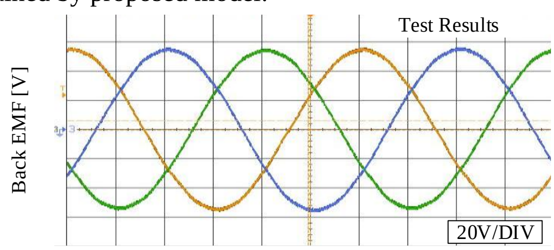

(a)

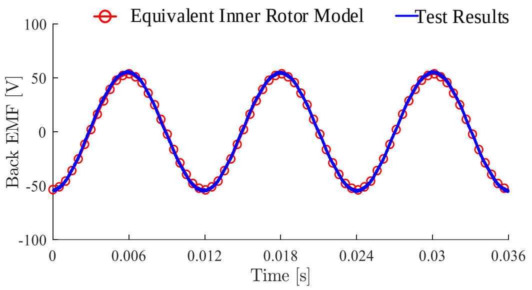

(b)

FIGURE 11. (a) Test rig. (b) Comparison between the test results and the proposed calculation method.

VII. Conclusion

In this article, we presented the first reported analytical solution based on pairs of coils in Cartesian coordinates. in the SD model, PMs and the air-gap are combined into a single region, which results in reduced unknown coefficients, resulting in a reduced-order solving matrix and simplifying the design procedure. This is a significant advantage for this approach, the workload is reduced with a great extent. The theoretical derivation of current densities of PMs sides are given in detail.

Although this first successful attempt for AFPM machines with the proposed approach, and one of main assumptions is that the iron has infinite permeability, which means the saturation is not considered in proposed model. This can be solved by incorporating the proposed method in elementary SD or harmonic SD, alternative approach to solve magnetic saturation is to work with simple magnetic circuit model.

Overall, the method in this paper provides a solid base for further studies. The proposed theory can be used in other SD models, which can consider the saturation and calculate the iron loss.

REFERENCES

[1] N. J. Stannard, J. G. Washington, and G. J. Atkinson, ‘A comparison of axial field topologies employing SMC for traction applications’, in *2016 19th International Conference on Electrical Machines and Systems (ICEMS)*, 2016, pp. 1–6.

[2] J. Yu, C. Liu, S. Liu, and H. Zhao, ‘Comparative Study of Double-Stator Interior-PM Vernier Machines Based on Electromagnetic-Structural Coupling Analysis’, *IEEE Transactions on Industrial Electronics*, vol. 68, no. 11, pp. 10510–10520, Nov. 2021, doi: 10.1109/TIE.2020.3034848.

[3] H. Vansompel, P. Sergeant, L. Dupré, and A. V. den Bossche, ‘Axial-Flux PM Machines With Variable Air Gap’, *IEEE Transactions on Industrial Electronics*, vol. 61, no. 2, pp. 730–737, Feb. 2014, doi: 10.1109/TIE.2013.2253068.

[4] H. Hu, X. Liu, J. Zhao, and Y. Guo, ‘Analysis and Minimization of Detent End Force in Linear Permanent Magnet Synchronous Machines’, *IEEE Transactions on Industrial Electronics*, vol. 65, no. 3, pp. 2475–2486, Mar. 2018, doi: 10.1109/TIE.2017.2740851.

[5] S. Andersson, ‘Optimization of a servo motor for an industrial robot application’, Lund Univ., Lund, 2000.

[6] P. Moreton, *Industrial brushless servomotors*. Newnes, 1999. Accessed: Aug. 15, 2016. [Online]. Available: http://books.google.com/books?hl=en&lr=&id=Ai_coOUaiOcC&oi=fnd&pg=PP1&dq=%22a+detailed+treatment+of+control+techniques+which%22+%22and+so+both+forms+are+explained+from+first%22+%22and+mechanical+properties+which+are%22+%22of+Bristol,+and+wish+to+acknowledge+here+the%22+&ots=AJMX-jd1sY&sig=55lRuBdKa8ll97RddWbzPUpYDV4

[7] M. Hajdinjak and D. Miljavec, ‘Analytical Calculation of the Magnetic Field Distribution in Slotless Brushless Machines With U-Shaped Interior Permanent Magnets’, *IEEE Transactions on Industrial Electronics*, vol. 67, no. 8, pp. 6721–6731, Aug. 2020, doi: 10.1109/TIE.2019.2939967.

[8] F. Dubas and K. Boughrara, ‘New Scientific Contribution on the 2-D Subdomain Technique in Polar Coordinates: Taking into Account of Iron Parts’, *Mathematical and Computational Applications*, vol. 22, no. 4, p. 42, Oct. 2017, doi: 10.3390/mca22040042.

[9] F. Dubas and K. Boughrara, ‘New Scientific Contribution on the 2-D Subdomain Technique in Cartesian Coordinates: Taking into Account of Iron Parts’, *Mathematical and Computational Applications*, vol. 22, no. 1, p. 17, Feb. 2017, doi: 10.3390/mca22010017.

[10] F. Farrokh, A. Vahedi, H. Torkaman, M. Banejad, and V. Z. Faradonbeh, ‘A 2D hybrid analytical electromagnetic model of the dual-stator axial-field flux-switching permanent magnet motor’, *IET Electric Power Applications*, vol. 18, no. 2, pp. 252–264, 2024, doi: 10.1049/elp2.12385.

[11] F. Farrokh, A. Vahedi, H. Torkaman, M. Banejad, and V. Zamani Faradonbeh, ‘Fast 2-D Analytical Model for Axial-Field Flux-Switching Bar-Permanent Magnet Motor’, *IEEE Transactions on Magnetics*, vol. 60, no. 8, pp. 1–12, Aug. 2024, doi: 10.1109/TMAG.2024.3416176.

[12] Y. Ni, K. Chen, B. Xiao, W. Qian, and Q. Wang, ‘Analytical Modeling of PM Electrical Machines With Eccentric Surface-Inset Halbach Magnets’, *IEEE Trans. Magn.*, vol. 57, no. 4, pp. 1–9, Apr. 2021, doi: 10.1109/TMAG.2021.3058095.

[13] D. Golovanov and C. Gerada, ‘An Analytical Subdomain Model for Dual-Rotor Permanent Magnet Motor With Halbach Array’, *IEEE Transactions on Magnetics*, vol. 55, no. 12, pp. 1–16, Dec. 2019, doi: 10.1109/TMAG.2019.2941699.

[14] L. Wu and Z. Q. Zhu, ‘Analytical Modeling of Surface-Mounted PM Machines Accounting for Magnet Shaping and Varied Magnet Property Distribution’, *IEEE Transactions on Magnetics*, vol. 50, no. 7, pp. 1–11, Jul. 2014, doi: 10.1109/TMAG.2014.2304272.

[15] Y. Zhou, H. Li, G. Meng, S. Zhou, and Q. Cao, ‘Analytical Calculation of Magnetic Field and Cogging Torque in Surface-Mounted Permanent Magnet Machines Accounting for Any Eccentric Rotor Shape’, *IEEE Transactions on Industrial Electronics*, pp. 3438–3447, 2014, doi: 10.1109/TIE.2014.2369458.

[16] B. Guo, Y. Huang, F. Peng, and J. Dong, ‘General Analytical Modeling for Magnet Demagnetization in Surface Mounted Permanent Magnet Machines’, *IEEE Transactions on Industrial Electronics*, vol. 66, no. 8, pp. 5830–5838, Aug. 2019, doi: 10.1109/TIE.2018.2873099.

[17] B. Guo *et al.*, ‘Nonlinear Semi-Analytical Model for Axial Flux Permanent-Magnet Machine’, *IEEE Transactions on Industrial Electronics*, pp. 1–1, 2022, doi: 10.1109/TIE.2022.3159952.

[18] B. Guo, Y. Huang, F. Peng, J. Dong, and Y. Li, ‘Analytical Modeling of Misalignment in Axial Flux Permanent Magnet Machine’, *IEEE Transactions on Industrial Electronics*, vol. 67, no. 6, pp. 4433–4443, Jun. 2020, doi: 10.1109/TIE.2019.2924607.

[19] L. Wu, H. Yin, D. Wang, and Y. Fang, ‘On-Load Field Prediction in SPM Machines by a Subdomain and Magnetic Circuit Hybrid Model’, *IEEE Transactions on Industrial Electronics*, vol. 67, no. 9, pp. 7190–7201, Sep. 2020, doi: 10.1109/TIE.2019.2942561.

[20] T. Lubin, S. Mezani, and A. Rezzoug, ‘Development of a 2-D Analytical Model for the Electromagnetic Computation of Axial-Field Magnetic Gears’, *IEEE Transactions on Magnetics*, vol. 49, no. 11, pp. 5507–5521, Nov. 2013, doi: 10.1109/TMAG.2013.2267746.

This article has been accepted for publication in IEEE Access. This is the author's version which has not been fully edited and
content may change prior to final publication. Citation information: DOI 10.1109/ACCESS.2025.3618398

Qilong Xue was born in 1983. He received the bachelor's degree in electrical engineering and the Ph.D. degree in drilling engineering from the China University of Petroleum (East), in 2006 and 2014, respectively. He has been worked at China Petroleum Ltd., from 2006 to 2008. He has been engaged in research on measurement and control technology of drilling engineering. From September 2012 to September 2013, he was a Joint Researcher at the University of Calgary, where he focuses on research of real time measurement of bottom drilling tool's attitude and rotary steerable drilling systems. He is currently an Associate Professor with the China University of Geosciences

Pengpeng Huang was born in Qingdao. She received the master's degree from the Shandong University of Science and Technology in 2014. She is currently an worker with the Nanjing Normal University, Nanjing, China in 2021.

Frédéric Dubas was born in Vesoul (France, 1978). He received the M.Sc. degree and the Ph.D. degree from the "Univ. Bourgogne Franche-Comté" (Besançon, France) in 2002 and 2006, respectively, with a focus on the design and the optimization of high-speed surface-mounted permanent-magnet (PM) synchronous motor for the drive of a fuel cell air-compressor.

From 2014 to 2016, he has been the Head of "Unconventional Thermal and Electrical Machines" Team. He is the Head of the "Electrical Actuators" group in the "Hybrid & Fuel Cell Systems, Electrical Machines (SHARPAC)" Team. He works with ALSTOM Transports (Ornans, France), and RENAULT Technocenter (Guyancourt, France), where he is involved in the modelling, design and optimization of electrical systems and, in particular, induction and PM synchronous (radial and/or axial flux) machines, creative problem solving, and electrical propulsion/traction. He is currently an Associate Professor with the Dpt. ENERGIE, , CNRS, Institut FEMTO-ST.

He has authored over 100 refereed publications and he holds a patent about the manufacturing of axial-flux PM machines with flux-focusing. Dr. Dubas received: i) Prize Paper Award (IEEE VPPC, 2005), ii) Prize Presentation Award (WASET ICEMS, 2017), iii) RENAULT Internal Award (Direction Engineering Alliance – Innovation – 2019), iv) Best Paper Award (IEEE ICEMS, 2021).

Baocheng Guo received the B.E. degree in electrical engineering from China university of petroleum, Qingdao, China, in 2009, M.E. degree in electrical engineering from Harbin university of science and technology, Harbin, China, in 2014, and Ph.D. degree in electrical engineering from Southeast university, Nanjing, China in 2017.

He is currently an Assistant Professor at the Nanjing Normal University since 2020. Before joining NNU, he was a post-doc researcher at Southeast university. His main interests are the electromagnetic field computation, and development of fast multiphysics models of electrical machines.